

## Phase-change-material-based flexible metasurfaces for electrically tuned broadband infrared image steganography

Yu Liu, Jun-Xuan Chen, Ben-Qi Hou, Yu-Tong Xiao, Bo Xiong, Jia-Nan Wang, Xing-Yuan Huo,  
Ru-Wen Peng<sup>✉\*</sup>, and Mu Wang<sup>✉†</sup>

*National Laboratory of Solid State Microstructures, School of Physics, Collaborative Innovation Center of Advanced Microstructures, and Jiangsu Physical Science Research Center, Nanjing University, Nanjing 210093, China*

(Received 23 August 2024; revised 13 November 2024; accepted 13 December 2024; published 21 January 2025)

Dynamic control of image display plays a crucial role in many infrared applications, particularly in infrared image steganography and thermal camouflage. In this paper, we experimentally demonstrate flexible and electrically tunable metasurfaces for infrared image steganography through dynamic polarization conversion in a broadband regime. Our metasurface consists of an array of gold nanobricks deposited on a thin film of vanadium dioxide ( $\text{VO}_2$ ). The electrical tunability is achieved by actively controlling the phase transition of  $\text{VO}_2$ . By modulating the applied current, the metasurface can be dynamically and reversibly tuned from a half-wave plate to a mirror across a broadband infrared regime. Furthermore, the flexibility of the metasurface enables operation even in bent states. We showcase the application of these flexible and electrically tunable metadevices for infrared image display. By encoding intensity images into the orientation of the nanobricks within the metasurface, we demonstrate the reversible hiding or displaying of infrared images through electrical tuning. This dynamic process effectively serves as infrared image steganography, offering tunable concealment capabilities for sensitive information. Our results reveal potential applications in conformal infrared target simulation, flexible anticontrol, and wearable thermal camouflage devices. Additionally, our strategy for dynamic tuning highlights promising pathways for future developments in reconfigurable device technology.

DOI: 10.1103/PhysRevApplied.23.014039

### I. INTRODUCTION

Image display at infrared frequencies is of great significance for various fields, encompassing infrared target simulation [1], camouflage [2,3], and anticontrol measures [4]. This functionality hinges on precisely controlling output intensity at spatial resolutions, typically facilitated by devices like metasurfaces. Metasurfaces, consisting of arrays of artificial meta-atoms, offer a powerful platform for manipulating the properties of electromagnetic waves at subwavelength scales [5–9]. Infrared metasurfaces enable image display by spatially arranging meta-atoms with distinct optical responses [10–12]. However, conventional passive metasurfaces possess fixed functionalities upon fabrication. Hence, a pressing need arises for dynamically controlled image display devices for diverse information applications.

Recently, the integration of metasurfaces with dynamically tunable materials, such as graphene [13], indium tin oxide [14,15], liquid crystals [16–19], and phase-change

materials [20–35], has enabled dynamic control over the optical responses of metadevices. Notably, phase-change materials offer an attractive option for infrared image display due to their extensive dynamic range of optical properties. For instance, combining vanadium dioxide ( $\text{VO}_2$ ) with metastructures facilitates adaptive camouflage [28] and active infrared display [29]. Moreover,  $\text{Ge}_3\text{Sb}_2\text{Te}_6$ -based infrared Huygens' metasurfaces allow for optical programming of spatial light phase distribution and retrieving high-resolution phase-encoded images [30]. The metasurface made of  $\text{Sb}_2\text{S}_3$  meta-atoms has been demonstrated theoretically for dynamic infrared holographic imaging at resonant wavelengths based on the geometry phase of quasi-bound states in the continuum [31].

On the other hand, flexible optical devices have presented significant development to fulfill functions that rigid platforms cannot provide [36]. Metasurfaces engineered on flexible substrates [37–39] have ushered in new possibilities for applications like wearable sensors [40], active absorbers [41], flexible photodetectors [42], and optical cloaking [43]. Notably, metadevices designed for dynamic image display could benefit significantly from incorporating mechanical flexibility. Nevertheless, the prevailing

\*Contact author: rwpeng@nju.edu.cn

†Contact author: muwang@nju.edu.cn

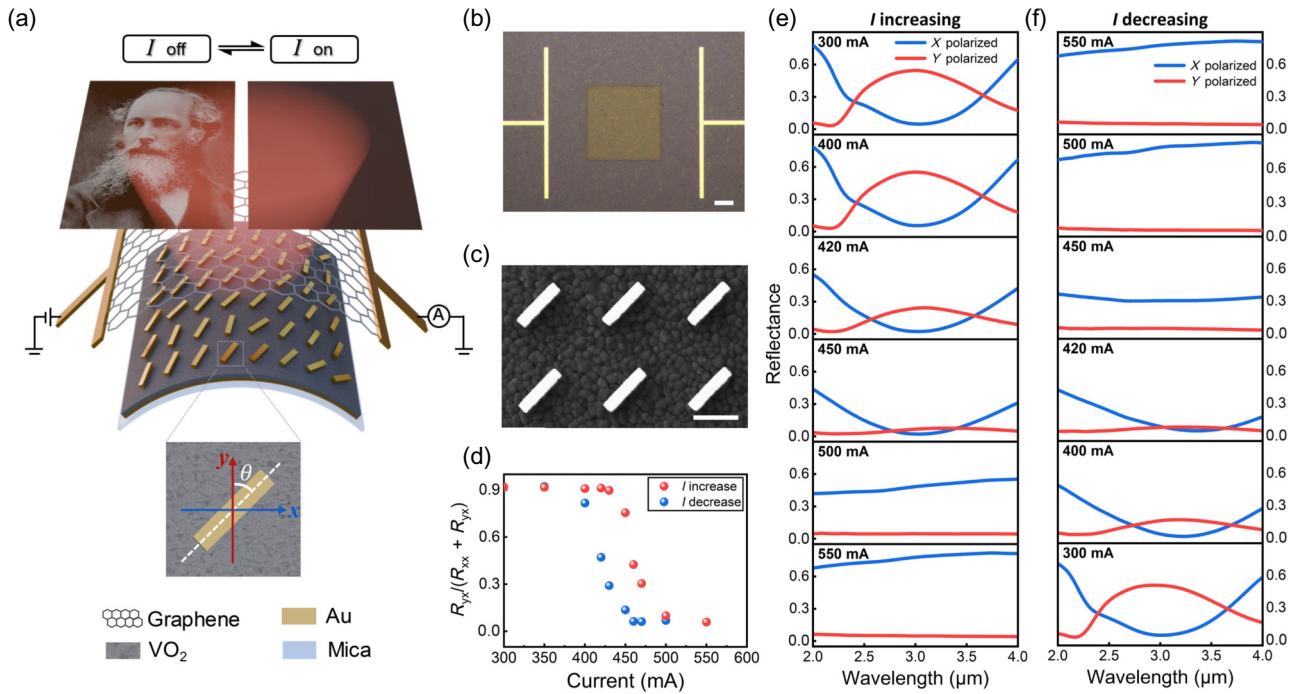


FIG. 1. Design of the electrically tuned infrared metasurface, sample fabrication, and optical characterization. (a) Schematic of a flexible and electrically tuned infrared metasurface consisting of an Au reflecting layer on a mica substrate, a  $\text{VO}_2$  spacing layer, and an Au nanobrick array covered with a thin graphene film. Also shown is the unit cell of a nanobrick rotated at  $45^\circ$ . (b) Optical micrograph of the Au nanobrick array. The scale bar is  $50 \mu\text{m}$ . (c) SEM micrograph of the fabricated sample. The scale bar is  $450 \text{ nm}$ . (d) Variation of the polarization conversion efficiency as a function of the applied current. (e),(f) The measured reflection spectra of the sample when the applied current (e) increases from 300 to 550 mA and (f) decreases from 550 to 300 mA.

flexible substrates, typically crafted from polymer materials [37,44], operating below 500 K due to thermal instability, present compatibility hurdles with the fabrication process of phase-change materials, which require high temperatures surpassing 500 K. Mica sheet, a smooth, chemically inert substrate with excellent flexibility and high-temperature stability, has been utilized for flexible and dynamic metadevices [41,45,46].

In this work, we demonstrate a flexible and electrically tunable metasurface for dynamic image display through polarization conversion in the infrared regime. As shown schematically in Fig. 1(a), we choose a thin mica sheet as a substrate to make a flexible film of phase-change material  $\text{VO}_2$ . The metasurface, which consists of an array of gold nanobricks, is fabricated on this flexible film. Here the  $\text{VO}_2$  film serves as a crucial space layer between the gold mirror and nanostructures, simultaneously enabling electrical tunability. By applying an electric current on the metadevice, the phase transition of  $\text{VO}_2$  film can be tuned. Then we experimentally demonstrate that this flexible and electrically tunable  $\text{VO}_2$ -based metasurface can be applied for dynamic polarization conversion in the broadband infrared regime. Furthermore, we extend our approach to dynamic infrared image display. The experiments show the reversible hiding or displaying of infrared

images through electrical tuning, effectively functioning as dynamic flexible broadband infrared image steganography.

## II. RESULTS AND DISCUSSION

### A. Design of the flexible and electrically tuned infrared metasurface

We designed and fabricated an electrically tuned infrared metasurface based on the phase-change material  $\text{VO}_2$ , which has an insulator-metal transition around a critical temperature of  $68^\circ\text{C}$ , corresponding to structural variation from the monoclinic phase to the rutile one [22,23]. The designed metasurface consists of a gold nanobrick array on a 200-nm-thick  $\text{VO}_2$  film, sitting upon a 100-nm-thick gold film on a mica substrate. By using the finite-difference time-domain method (FDTD Solutions, Lumerical Inc.), the reflective amplitude and phase of a  $\text{VO}_2$ -based metasurface, together with its polarization-dependent reflection spectra, are simulated as shown in Appendix A, where the  $45^\circ$ -oriented gold nanobrick is 500 nm in length, 100 nm in width, and 100 nm in height, and the nanobrick array has a spatial periodicity of 800 nm. When  $\text{VO}_2$  is in the dielectric phase,  $x$ -polarized incident light is turned to  $y$ -polarized reflected light in the wavelength range from 2.5 to  $4 \mu\text{m}$ , indicating that the

metasurface acts as a broadband infrared half-wave plate. The performance of the half-wave plate can be further improved by replacing part of the VO<sub>2</sub> layer with an SiO<sub>2</sub> layer. The absorption of the overall structure can be reduced. Once VO<sub>2</sub> is in the metallic phase, the polarization of the reflected light remains the same as that of the incident light, indicating that the metasurface acts as a broadband infrared mirror.

Such a VO<sub>2</sub>-based metasurface is fabricated to verify the dynamic polarization conversion experimentally. A 100-nm-thick gold film was first deposited on a freshly cleaved, flexible mica sheet. Then, a 200-nm-thick VO<sub>2</sub> film was fabricated sequentially using electron-beam evaporation and annealing in an oxygen atmosphere at 430–470 °C. Because of the excellent fabrication compatibility of VO<sub>2</sub> film on the flexible and heat-resistant mica substrate, a smooth and flexible phase-change material can be achieved. The spectral responses of the fabricated VO<sub>2</sub> film versus temperature are shown in Appendix B, demonstrating the excellent quality of the flexible phase-change material. Then, gold nanostructures 100 nm in thickness were fabricated by electron-beam lithography and a lift-off process. A pair of T-shaped gold electrodes were simultaneously fabricated to realize the electrical tunability of the metasurface.

An optical micrograph of the sample is illustrated in Fig. 1(b), where the total size of the sample in the field of view reaches 200 × 200 μm<sup>2</sup>. Figure 1(c) shows the scanning electron microscopy (SEM) image of the Au nanobrick array on the VO<sub>2</sub> film. Furthermore, the Au nanostructure together with the T-shaped gold electrodes were covered with a layer of graphene, which provides Joule heating for the phase transition of VO<sub>2</sub> by applying an electrical current across the sample. The monolayer graphene film has a negligible influence on the optical response of the overall structure [47,48]. The details are discussed in Appendix C. A dc source with a built-in ammeter was connected to the electrodes to accurately apply the electric current to the graphene film.

## B. Electrical tunability of the VO<sub>2</sub>-based metasurface as an infrared half-wave plate

We then conducted optical measurements of the VO<sub>2</sub>-based metasurface at various applied currents using a Fourier-transform infrared spectrometer (Vertex 70v, Bruker), as illustrated in Figs. 1(e) and 1(f). Firstly, with different applied electric currents, we measured the reflection spectra of the VO<sub>2</sub>-based metasurface under *x*-polarized incidence at wavelengths ranging from 2 to 4 μm. The reflectance is defined as the ratio of reflected light intensity to the intensity of the incident light. When the applied current *I* is below 300 mA, the VO<sub>2</sub> film remains in the dielectric phase. Meanwhile, the VO<sub>2</sub>-based

metasurface serves as a half-wave plate, leading to a polarization rotation of 90°.

The typical reflection spectrum is shown in the top panel of Fig. 1(e). The wavelength range of polarization conversion observed in the experiments is narrower than that predicted by simulation, primarily due to fabrication imperfections, including variations in the VO<sub>2</sub> film thickness and deviations in the length, width, and height of the gold nanobricks. When the applied current increases from 300 to 550 mA, the induced Joule heating triggers a phase transition in VO<sub>2</sub>. The reflection spectrum measurements are taken at several stable intermediate states in the phase transition process. As shown in Fig. 1(e), there is a significant decrease in *y*-polarized reflectance initially, while the *x*-polarized reflectance reduces slightly until the absorption of the VO<sub>2</sub>-based metasurface reaches its maximum. This phenomenon comes from the gradual transformation of VO<sub>2</sub> from the dielectric state to the metallic one. As the applied current increases, the *y*-polarized reflectance of the VO<sub>2</sub>-based metasurface remains at zero while the *x*-polarized reflectance increases rapidly. Upon the applied current surpassing 550 mA, both *x*- and *y*-polarized reflectances stop changing, indicating that the VO<sub>2</sub> film has completely transformed into a metallic phase. Meanwhile, the reflectance is all *x*-polarized and reaches around 0.7 at a wavelength ranging from 2 to 4 μm, indicating that the metasurface with metallic VO<sub>2</sub> operates as a broadband infrared mirror.

It should be noted that the electrical tunability of the VO<sub>2</sub>-based metasurface is reversible. The reflection spectra of this metasurface are also measured when the applied electric current is decreased from 550 to 300 mA, as shown in Fig. 1(f). The *x*-polarized reflectance decreases first. Then the *y*-polarized component increases until the reflectance returns to the initial scenario at 300 mA [see the first plot in Fig. 1(e)].

Throughout the entire cycle of increasing and decreasing the electric current, we can extract the polarization conversion efficiency, for example, at a wavelength of 3 μm, and plot its variation with respect to the applied current, as shown in Fig. 1(d). Here, the polarization conversion efficiency is defined as  $R_{yx}/(R_{yx} + R_{xx})$ , where  $R_{yx}$  is *y*-polarized reflectance and  $R_{xx}$  is *x*-polarized reflectance both under *x*-polarized incidence, respectively. The variations of the polarization conversion efficiency as a function of the applied current exhibited a hysteresis feature, which originates from the intrinsic hysteresis of the VO<sub>2</sub> phase transition process. The nucleation process during the phase transition differs in the current-up and current-down scenarios [49]. These experimental measurements show a continuous and reversible modulation of the output polarization state based on the electrically tuned VO<sub>2</sub>-based metasurface. In addition, the time response of the electrically tuned VO<sub>2</sub>-based metasurface is also examined, as shown in Appendix D. The measured ON and OFF

switching times for 0.1-Hz square-wave current are 36 and 52 ms, respectively.

### C. Mechanical flexibility of the electrically tuned infrared metasurface

Such infrared metasurfaces can also work on various curved substrates due to their insensitive optical responses to the incident angle, as presented in Appendix E. Now we study the effect of bending of the mica substrate on the performance of the VO<sub>2</sub>-based metasurface to testify to its mechanical flexibility. The degree of bending for the flexible substrate can be characterized by its radius of curvature. The bending radius ( $r$ ) is evaluated by

$$d = 2r \sin \frac{l}{2r}, \quad (1)$$

where  $d$  and  $l$  represent the measured chord length of the bending substrate and the side length of the flat substrate, respectively. Here, the side length of the thin mica film is 15 mm. To bend the mica thin film accurately, we applied a push force at both ends, as shown in Fig. 2(a).

In our experiments, we set the flexible sample to various bending radii. We measured the reflection spectra of the sample in different bending states when the applied current was 0 and 550 mA, as shown in Figs. 2(c) and 2(d),

respectively. It can be observed that the reflective  $x$ - and  $y$ -polarized components do not vary significantly when the bending radius changes from 19 to 9 mm. Moreover, the polarization conversion efficiencies extracted from the reflection spectra of the metasurface at different bending radii are represented by red and blue dots for the applied currents of 0 and 550 mA, respectively, in Fig. 2(b). These results are in good agreement with the simulation under oblique incidence presented in Appendix E. Furthermore, the bending durability of these flexible structures is demonstrated in Appendix F. The spectral response of the VO<sub>2</sub> film in both its dielectric and metallic phases shows no significant variation after 500 bending cycles. With these results, we experimentally demonstrated the capability of VO<sub>2</sub>-based metasurface to electrically tune polarization conversion in bending conditions.

### D. Dynamic infrared image steganography based on a flexible and electrically tuned VO<sub>2</sub>-based metasurface

Based on the electrically tunable and flexible VO<sub>2</sub>-based metasurface, we further demonstrate the reversible and continuous modulation of gray-scale imaging on a flexible substrate. When incident light passes through a polarizer along the  $x$  direction, interacts with a metasurface functioning as a half-wave plate, and is subsequently analyzed

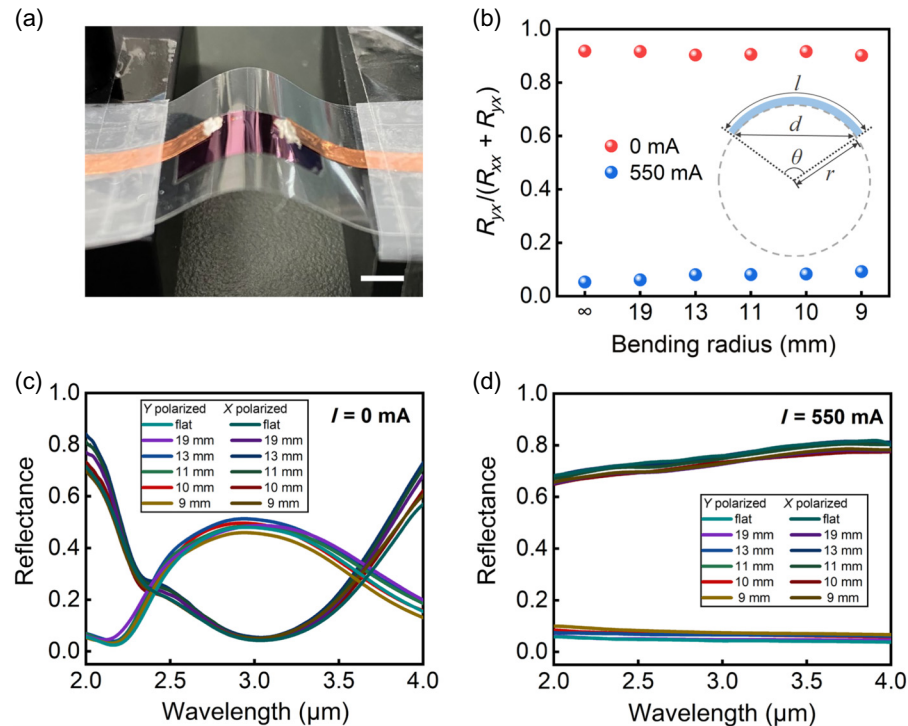


FIG. 2. (a) Photograph of the flexible and electrically tuned infrared half-wave plate. The scale bar is 4 mm. (b) Measured polarization conversion efficiency of the metasurface at a wavelength of 3  $\mu\text{m}$  as a function of bending radius when the applied current is 0 and 550 mA. Inset: Schematic of the bending process. The blue layer represents the flexible substrate and the bending radius is solved by  $d = 2r \sin(l/2r)$ . (c),(d) Measured reflection spectra of the flexible and electrically tuned infrared half-wave plate in the flat state and different bent states with bending radii from 19 to 9 mm when the applied current is (c) 0 mA and (d) 550 mA.

by a polarization analyzer aligned in the  $y$  direction, the output intensity of the reflected light satisfies Malus' law,

$$I = I_0 \sin^2(2\theta), \quad (2)$$

where  $I_0$  is the intensity of the incident light and  $\theta$  is the in-plane orientation of the nanobrick (details can be found in Appendix G). According to Eq. (2), the output intensity can be continuously controlled from 0 to  $I_0$  by rotating the orientation of the nanobrick from  $0^\circ$  to  $45^\circ$ .

For the experimental sample design, we chose 10 distinct orientations of the nanobricks. This selection accommodated the precision required for experimental fabrication and measurements. Subsequently, we fabricated 10 different VO<sub>2</sub>-based metasurfaces, each comprising arrays of nanobricks with a specific orientation. The reflection spectra of these 10 samples are measured when the applied current is 0 and 550 mA, respectively. The solid curves in Fig. 3(a) show the case of zero applied current. As the rotation angle of the nanobricks decreases from  $45^\circ$  to  $0^\circ$ , the reflectance for  $y$ -polarized light gradually diminishes, while that for  $x$ -polarized light gradually increases. Further, we extracted the polarized reflectance at a wavelength of 3  $\mu\text{m}$  across various rotation angles, as plotted in Fig. 3(b), with red and blue dots representing  $x$ - and  $y$ -polarized reflectance, respectively. The solid red and blue curves denote the theoretical intensity derived from Eq. (2), showcasing a commendable agreement between the measured and theoretical results. The distinct reflectance as a function of the rotation angle of the nanobrick [as shown in Fig. 3(b)] makes it possible to use these 10 nanobricks to encode gray-scale images.

Upon applying a current of 550 mA, VO<sub>2</sub> turns to the metallic phase, and all 10 metasurfaces act as polarization-independent infrared mirrors. Their reflection spectra are illustrated as the dotted red or blue curves in Fig. 3(a). The extracted reflectance at 3  $\mu\text{m}$  wavelength versus the rotation angle of the nanobrick is given in Fig. 3(c). Notably, the  $x$ - and  $y$ -polarized reflectances remain nearly constant at different rotation angles of the nanobrick, which indicates that the gray-scale image embedded within the VO<sub>2</sub>-metasurface will disappear when sufficient electrical current is applied. Therefore, we are ready to make a gray-scale image embedded in the metasurface, visible only when VO<sub>2</sub> is in the dielectric phase and invisible when VO<sub>2</sub> is in the metallic phase.

Further, we design and fabricate an electrically tuned flexible metadevice for dynamic infrared image display. Here we chose a gray-scale portrait of James C. Maxwell as the target image. In the design, we discretized the intensity of the target gray-scale image and then meticulously mapped it onto the orientation of each nanobrick pixel by pixel. This approach yielded the requisite orientation distribution of nanobricks across the metasurface. Subsequently, the metasurface was fabricated using standard

electron-beam lithography techniques. Figure 3(d) illustrates an SEM image of a portion of the fabricated sample, with the inset showing the optical micrograph.

The spatially resolved reflectance profile of the sample was measured using a Fourier-transform infrared spectrometer (Vertex 70v, Bruker) combined with an infrared microscope with a focal plane array (FPA) detector system (Hyperion 3000, Bruker). An FPA image can be collected by integrating the signals around the central wavelength [50–52]. The optical setup is schematically shown in Appendix H. The incident light was  $x$ -polarized, and the output light was analyzed with  $y$  polarization. Without applying electric current, the rotated nanobricks generated various output intensities.

In Fig. 3(e), the measured intensity profile of the sample in its flat state distinctly reveals the gray-scale image of Maxwell's portrait as intended. The incidence wavelength was 3  $\mu\text{m}$ . The relatively low resolution of the measured infrared image results from the FPA detection system. The FPA detector in our experiments images a region of  $200 \times 200 \mu\text{m}^2$  and generates a picture with  $256 \times 256$  resolution. The quality of measured infrared images was improved after image processing based on the histogram equalization method [53]. Upon applying the electric current, the evolution of the FPA image is depicted by red arrows in the upper row, illustrating the results achieved at 330 and 380 mA. Notably, as the applied electric current jumped up, the brightness and contrast of the FPA image gradually diminished, owing to the reduced intensity difference between rotated nanobricks. The encoded gray-scale image disappeared entirely once the applied current surpassed 440 mA. Conversely, by gradually decreasing the current, FPA images were measured at current values of 330 and 280 mA, as shown in the bottom row using blue arrows. Here, the contrast of the FPA image resumed as the applied current decreased.

Furthermore, we conducted similar measurements with the bent metadevice. As illustrated in Figs. 3(f) and 3(g), the FPA images closely resembled those obtained in the flat state at applied currents of 0 and 440 mA, demonstrating that bending of the metadevice does not noticeably affect the function of the display. These experimental observations confirm that an electrically tuned flexible metadevice for dynamic infrared image steganography has been realized.

To further illustrate the broadband property of the electrically tuned flexible metadevice, we conducted measurements of the FPA image across wavelengths from 2.8 to 3.2  $\mu\text{m}$ , as presented in Fig. 4. Notably, each rotated nanobrick exhibits a relatively broad operating bandwidth for polarization conversion. Consequently, the variation of output intensity regarding the different orientations of nanobricks remains valid. A clear image of Maxwell's portrait can be observed at each observation wavelength without applying an electric current. Once the current was

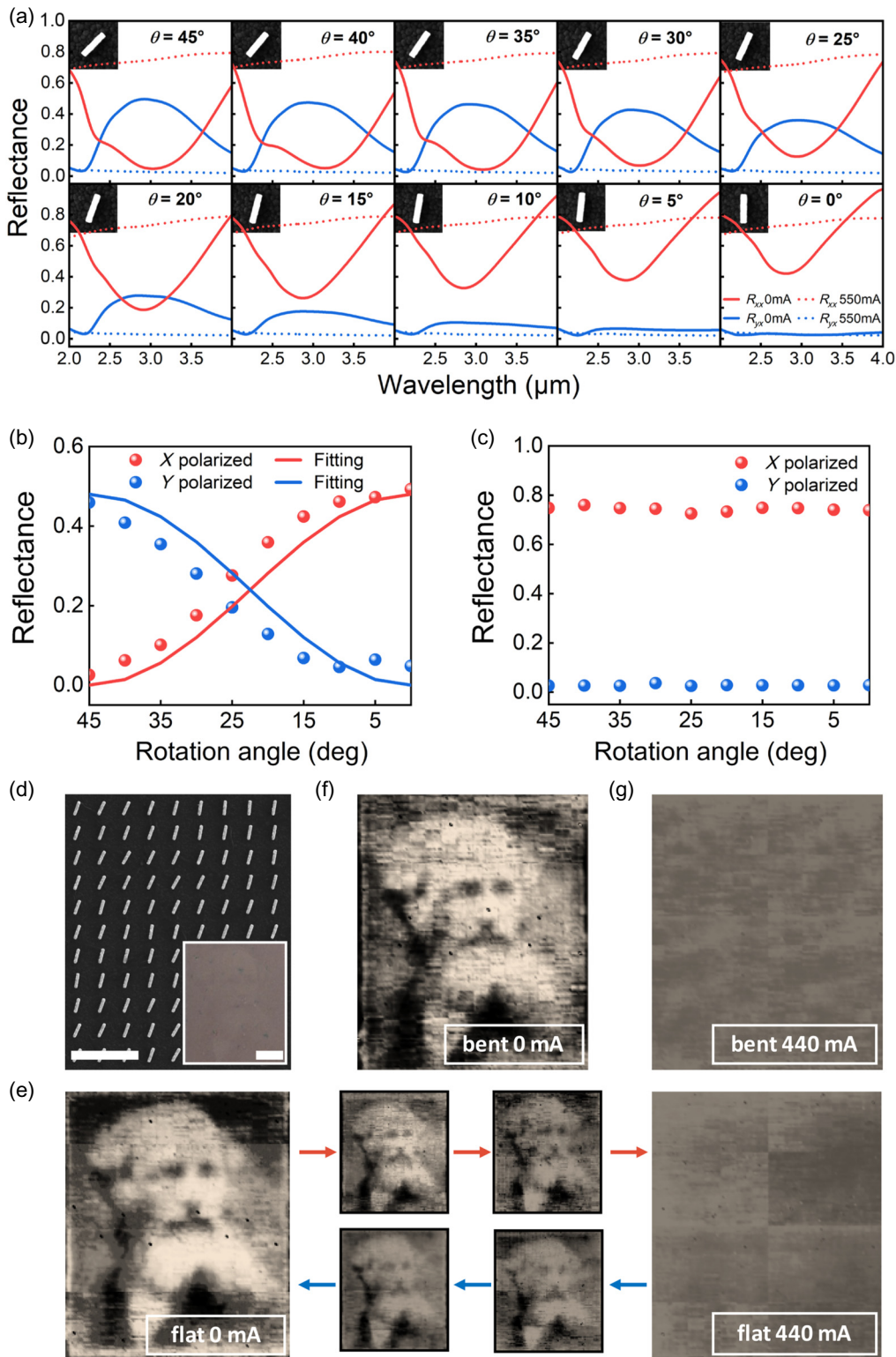


FIG. 3. (a) Measured reflection spectra of the nanobrick array with 10 different orientations from  $45^\circ$  to  $0^\circ$  when the applied current is 0 and 550 mA. The solid and dotted curves represent the results of 0 and 550 mA, respectively. The red and blue curves represent the  $x$ - and  $y$ -polarized reflectance. The inset (top left) is the SEM image of the corresponding rotated nanobrick. (b),(c) Measured reflectance of the nanobrick array at a wavelength of  $3\text{ }\mu\text{m}$  as a function of rotation angle when the applied current is (b) 0 mA and (c) 550 mA. (d) The SEM image of the sample for gray-scale imaging. The inset is the optical micrograph. The scale bar is 2  $\mu\text{m}$  and 100  $\mu\text{m}$ , respectively. (e) Focal plane array images of the sample in the flat state measured during increasing and decreasing applied currents. (f),(g) Focal plane array images of the sample in the bent state with a bending radius of 10 mm when the applied current is (f) 0 mA and (g) 440 mA.

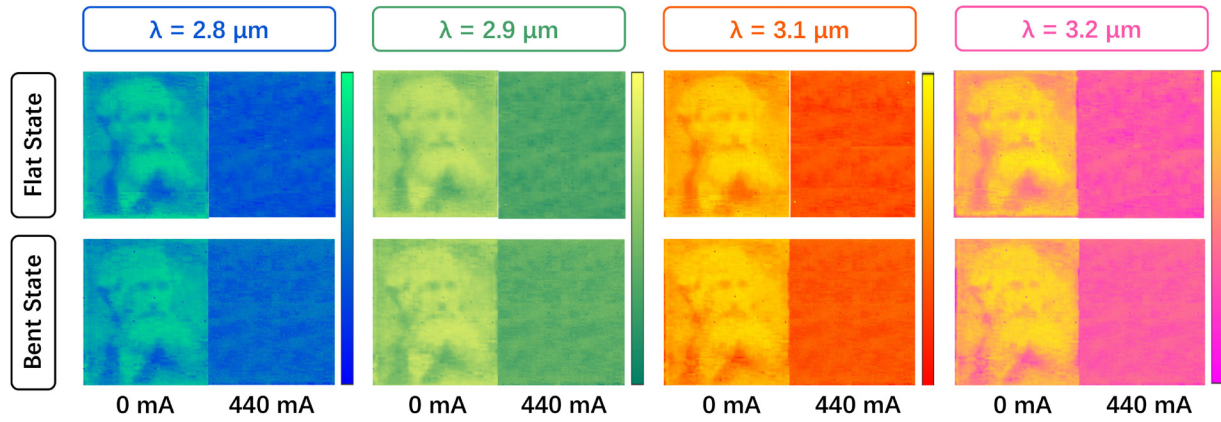


FIG. 4. Broadband responses of the metadevice for gray-scale imaging. The FPA images of the sample in the flat and bent states are measured at wavelengths of 2.8, 2.9, 3.1, and 3.2  $\mu\text{m}$  when the applied current is 0 and 440 mA. As shown, the metadevice exhibits high-contrast images in this wavelength range.

applied to a certain level, for instance, to 440 mA, the image of Maxwell's portrait disappeared completely. This phenomenon can be observed on both flat and bent samples. Therefore, the infrared images in both flat and bent states can be reversibly hidden or displayed by applying an electric current, which can serve as dynamic broadband infrared image steganography.

### III. CONCLUSION

In conclusion, we have demonstrated  $\text{VO}_2$ -based electrically tuned flexible metasurfaces for infrared image steganography via dynamic polarization conversion across a broadband regime. By precisely controlling the applied current, we could dynamically and reversibly tune the output polarization of the metasurface from the vertical to the horizontal state in a broadband infrared regime. The functionality of the metasurface has been stable across various bending states. Furthermore, by encoding the intensity image with the orientation of nanobricks of the metasurface, we demonstrated the capability of hiding and displaying the infrared images via electrical tuning. We suggest that this dynamic infrared image steganography strategy can be applied for adaptive infrared tagging, camouflaging, anticounterfeiting, and active wearable devices. Furthermore, our approach for dynamic tuning offers potential pathways for future developments in reconfigurable device technologies.

### ACKNOWLEDGMENTS

This work was supported by the National Key R&D Program of China (Grants No. 2022YFA1404303 and No. 2020YFA0211300), the National Natural Science Foundation of China (Grants No. 12234010, No. 61975078, and No. 11974177), and the Natural Science Foundation of Jiangsu Province (Grant No. BK20233001).

### APPENDIX A: SIMULATED REFLECTION SPECTRA OF THE UNIT CELL

Numerical simulations were carried out using the finite-difference time-domain method (FDTD Solutions, Lumerical Inc.). The amplitude and phase of the reflection of the nanobrick along the long and short axes were simulated. Figures 5(a) and 5(b) show the amplitude ratio and phase difference between the reflection along the long and short axes of the nanobrick, respectively. When the  $\text{VO}_2$  film was in the dielectric phase, the amplitude ratio was around unity, and the phase difference was around  $\pi$  in the wavelength range between 2.5 and 4  $\mu\text{m}$ . The device then acts as a half-wave plate. The phase difference becomes zero

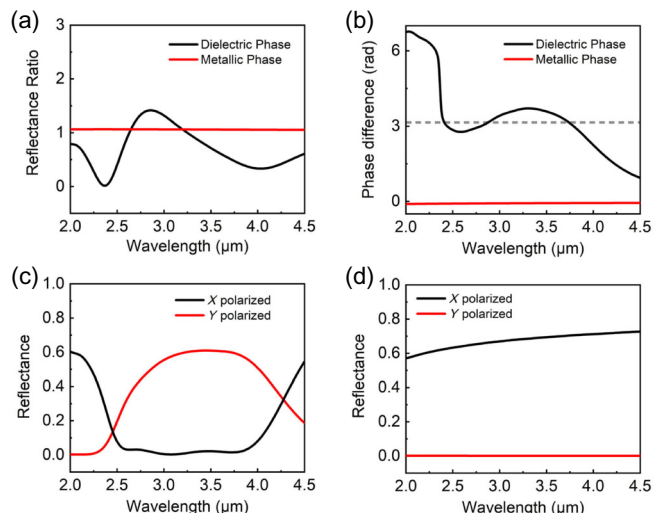


FIG. 5. (a) The simulated amplitude ratio and (b) phase difference between reflection along the long and short axes of the nanobrick. (c),(d) The simulated reflection spectra of the unit cell when the  $\text{VO}_2$  film was in the (c) dielectric and (d) metallic phase, respectively.

after the phase transition of the VO<sub>2</sub> film. Figures 5(c) and 5(d) demonstrate the simulated reflection spectra: the nanobrick in the unit cell was rotated by 45°, the incidence was *x*-polarized, and the VO<sub>2</sub> film was in the dielectric and metallic phases, respectively.

## APPENDIX B: SPECTRAL RESPONSE OF VO<sub>2</sub> VERSUS TEMPERATURE

We measured the infrared transmission spectra of a 200-nm-thick VO<sub>2</sub> film on a mica substrate at various temperatures during both the heating and cooling processes, as shown in Figs. 6(a) and 6(b), respectively. As observed, when the temperature increases within the range of 55–70 °C, the transmittance of the VO<sub>2</sub> film gradually decreases. Once the VO<sub>2</sub> film fully transitions to the metallic phase, its transmittance drops to near zero. During cooling, the transmission spectra gradually revert to their initial state, indicating the transformation of the VO<sub>2</sub> film back to its dielectric phase. These experimental results align with the reported critical phase transition temperatures (around 68 °C), confirming the high quality of the fabricated film.

## APPENDIX C: OPTICAL RESPONSE OF THE GRAPHENE LAYER

Based on the frequency-dependent optical sheet conductivity of monolayer graphene, its absorbance remains constant at 2.293% within the wavelength range of 2–2.5 μm. When the wavelength extends to 2.5–4 μm, the optical sheet conductivity decreases slightly, leading to a corresponding reduction in absorbance. To experimentally investigate the optical response of the graphene layer, we measured the transmission spectra of both the mica substrate alone and the graphene-covered mica, as shown in Fig. 7. The transmission spectrum between 2 and 4 μm shows no significant variation. When a sufficient current is applied, Joule heating in the graphene layer can drive the phase transition of the VO<sub>2</sub> film. Despite its presence, the monolayer graphene remains nearly transparent, exerting minimal influence on the transmission spectrum of the overall structure.

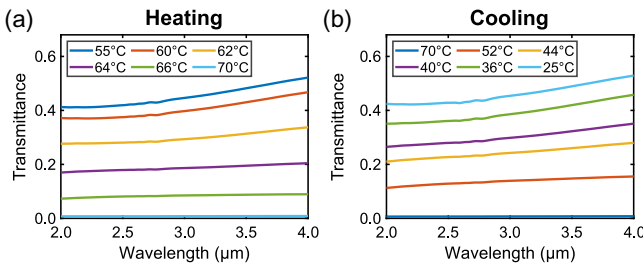


FIG. 6. The measured infrared spectra of a 200-nm-thick VO<sub>2</sub> film in the wavelength range from 2 to 4 μm during the (a) heating and (b) cooling process.

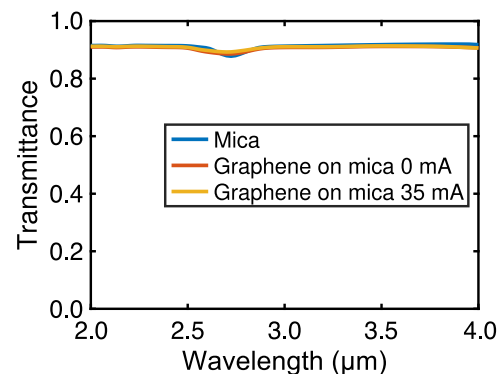


FIG. 7. The transmittance of the mica sheet, and of the graphene on the mica sheet with 0 and 35 mA applied current.

## APPENDIX D: TEMPORAL RESPONSE OF THE ELECTRICALLY TUNED METASURFACE

We used a time-domain reflection system to measure the temporal response of the sample at a wavelength of 2 μm. Rectangular current signals were applied to the graphene layer, with modulation frequencies set at 0.05, 0.1, 0.25, and 0.5 Hz. The results are shown in Fig. 8(a). Upon application of the current, the VO<sub>2</sub> film is transformed to its metallic phase, resulting in an increase in reflectance. The

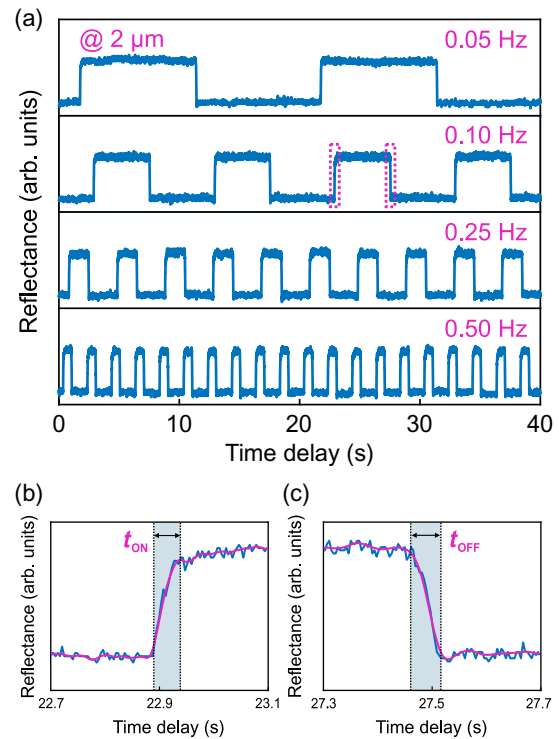


FIG. 8. (a) Temporal response of the electrically tuned phase transition of the 200-nm-thick VO<sub>2</sub> film measured at the wavelength of 2 μm. (b) A rising edge when the modulation frequency was 0.10 Hz. (c) A falling edge when the modulation frequency was 0.10 Hz.

reflectance returns to its initial value when the current is turned off. From the data at a modulation frequency of 0.1 Hz, we extracted a rising and a falling edge to determine the ON and OFF switching times ( $t_{\text{ON}}$  and  $t_{\text{OFF}}$ ), as shown in Figs. 8(b) and 8(c). The ON and OFF switching times are defined as the time for the reflectance to change from 10% to 90% of its maximum value and vice versa. Based on these criteria,  $t_{\text{ON}}$  and  $t_{\text{OFF}}$  are approximately 36 and 52 ms, respectively.

#### APPENDIX E: SIMULATED REFLECTION SPECTRA UNDER OBLIQUE INCIDENCE

Figure 9 demonstrates the simulated reflection spectra of the unit cell under the  $x$ -polarized incidence at different incident angles. Figures 9(a) and 9(b) show the  $y$ -polarized and  $x$ -polarized reflectance, respectively, when the  $\text{VO}_2$  film is in the dielectric phase. The function of polarization conversion is insensitive to the incident angle till  $40^\circ$ . Figures 9(c) and 9(d) present the  $y$ -polarized and  $x$ -polarized reflectance, respectively, when the  $\text{VO}_2$  film is in the metallic phase. These results also ensure that the device can work in the bent states. The results presented here are obtained with oblique incidence of TM waves. The results for oblique incidence of TE waves are similar.

#### APPENDIX F: BENDING DURABILITY OF THE FLEXIBLE STRUCTURE

To evaluate the bending durability of the flexible structure, we measured the spectra of the sample before and after 500 bending cycles. As shown in Figs. 10(a) and 10(b), the transmittance spectra of the 200-nm-thick  $\text{VO}_2$  film in its dielectric and metallic phases exhibit no

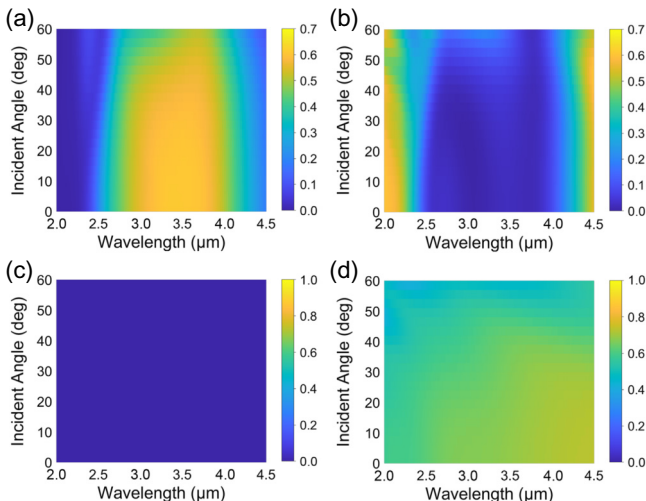


FIG. 9. The (a)  $y$ -polarized and (b)  $x$ -polarized reflectance when the  $\text{VO}_2$  film is in the dielectric phase. The (c)  $y$ -polarized and (d)  $x$ -polarized reflectance when the  $\text{VO}_2$  film is in the metallic phase.

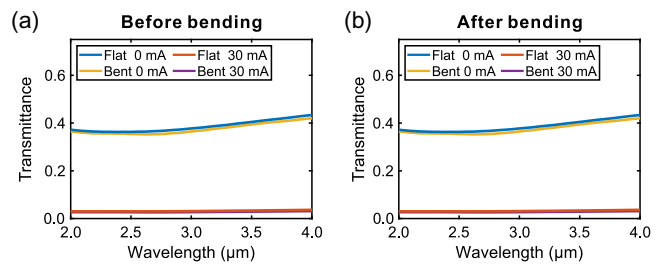


FIG. 10. Transmittance spectra of a 200-nm-thick  $\text{VO}_2$  film in the flat and bent states (a) before and (b) after bending 500 times.

significant changes after 500 bending cycles. The sample was bent to a radius of 10 mm. These results confirm the high reproducibility and stability of the graphene's performance under applied current.

#### APPENDIX G: DERIVATION OF EQUATION (2)

The Jones matrix of a unit cell containing a nanobrick with an in-plane rotation angle  $\theta$  can be expressed as

$$J = \begin{bmatrix} \cos \theta & -\sin \theta \\ \sin \theta & \cos \theta \end{bmatrix} \begin{bmatrix} A & 0 \\ 0 & B \end{bmatrix} \begin{bmatrix} \cos \theta & \sin \theta \\ -\sin \theta & \cos \theta \end{bmatrix}, \quad (\text{G1})$$

where  $A$  and  $B$  are complex reflection coefficients along the long and short axes, respectively, of the nanobrick in the unit cell for linearly polarized incidence. When normally incident light passes through a polarizer, a unit cell, and an analyzer in sequence, the electric field of the reflected light beam can be calculated by

$$E = \begin{bmatrix} \cos^2 \alpha_2 & \sin \alpha_2 \cos \alpha_2 \\ \sin \alpha_2 \cos \alpha_2 & \sin^2 \alpha_2 \end{bmatrix} \begin{bmatrix} \cos \theta & -\sin \theta \\ \sin \theta & \cos \theta \end{bmatrix} \times \begin{bmatrix} A & 0 \\ 0 & B \end{bmatrix} \begin{bmatrix} \cos \theta & \sin \theta \\ -\sin \theta & \cos \theta \end{bmatrix} \begin{bmatrix} A_0 \cos \alpha_1 \\ A_0 \sin \alpha_1 \end{bmatrix}, \quad (\text{G2})$$

where  $\alpha_1$  and  $\alpha_2$  are the transmission axis directions of the polarizer and the analyzer, respectively, and  $A_0$  is the amplitude of the incident light. Here, we choose  $\alpha_1 = 0$  and  $\alpha_2 = \pi/2$ . If the nanobrick acts as an ideal half-wave plate, the intensity of the reflected light can be expressed by

$$I = A_0^2 \sin^2(2\theta), \quad (\text{G3})$$

and the continuous output intensity from 0 to  $A_0^2$  can be obtained by rotating the nanobrick from  $0^\circ$  to  $45^\circ$ .

#### APPENDIX H: EXPERIMENTAL SECTION

For sample fabrication, a vanadium film was deposited onto an Au layer via electron-beam evaporation, followed by annealing in an oxygen atmosphere to achieve the  $\text{VO}_2$  phase. Gold nanobrick arrays, 100-nm thick, were then

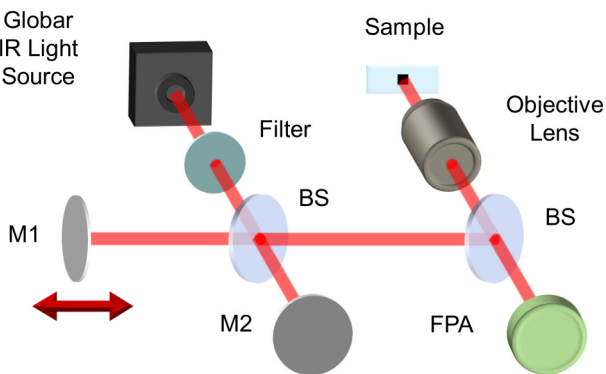


FIG. 11. The schematic of the setup: M1, moving mirror; M2, fixed mirror; BS, beam splitter; FPA, focal plane array.

fabricated on top of the Au/VO<sub>2</sub> layer using electron-beam lithography and lift-off techniques. The typical sample size is 200 × 200 μm<sup>2</sup>.

For optical measurements, reflection spectra were obtained using a Fourier-transform infrared system (Vertex 70v, Bruker). For focal plane array imaging, an infrared microscope with an FPA detection system (Hyperion 3000, Bruker) was used to capture infrared signals from the sample, as illustrated in Fig. 11. The FPA detector images an area of 200 × 200 μm<sup>2</sup>, producing a 256 × 256 resolution image.

- [1] O. M. Williams, Dynamic infrared scene projection: A review, *Infrared Phys. Technol.* **39**, 473 (1998).
- [2] S. Hong, S. Shin, and R. Chen, An adaptive and wearable thermal camouflage device, *Adv. Funct. Mater.* **30**, 1909788 (2020).
- [3] R. Hu, W. Xi, Y. Liu, K. Tang, J. Song, X. Luo, J. Wu, and C.-W. Qiu, Thermal camouflaging metamaterials, *Mater. Today* **45**, 120 (2021).
- [4] A. F. Smith and S. E. Skrabalak, Metal nanomaterials for optical anticounterfeit labels, *J. Mater. Chem. C* **5**, 3207 (2017).
- [5] N. Yu, P. Genevet, M. A. Kats, F. Aieta, J.-P. Tetienne, F. Capasso, and Z. Gaburro, Light propagation with phase discontinuities: Generalized laws of reflection and refraction, *Science* **334**, 333 (2011).
- [6] Y.-J. Gao, X. Xiong, Z. Wang, F. Chen, R.-W. Peng, and M. Wang, Simultaneous generation of arbitrary assembly of polarization states with geometrical-scaling-induced phase modulation, *Phys. Rev. X* **10**, 031035 (2020).
- [7] Q. Fan, M. Liu, C. Zhang, W. Zhu, Y. Wang, P. Lin, F. Yan, L. Chen, H. J. Lezec, Y. Lu, A. Agrawal, and T. Xu, Independent amplitude control of arbitrary orthogonal states of polarization via dielectric metasurfaces, *Phys. Rev. Lett.* **125**, 267402 (2020).
- [8] A. H. Dorrah, N. A. Rubin, A. Zaidi, M. Tamagnone, and F. Capasso, Metasurface optics for on-demand polarization transformations along the optical path, *Nat. Photonics* **15**, 287 (2021).
- [9] S. Wang, S. Wen, Z. L. Deng, X. Li, and Y. Yang, Metasurface-based solid Poincaré sphere polarizer, *Phys. Rev. Lett.* **130**, 123801 (2023).
- [10] M. Makhsyian, P. Bouchon, J. Jaeck, J.-L. Pelouard, and R. Haïdar, Shaping the spatial and spectral emissivity at the diffraction limit, *Appl. Phys. Lett.* **107**, 251103 (2015).
- [11] D. Franklin, S. Modak, A. Vázquez-Guardado, A. Safaei, and D. Chanda, Covert infrared image encoding through imprinted plasmonic cavities, *Light Sci. Appl.* **7**, 93 (2018).
- [12] Y. Cao, L. Tang, J. Li, C. Lee, and Z. Dong, Multiplexing optical images for steganography by single metasurfaces, *Small* **19**, 2206319 (2023).
- [13] Y. Yao, M. A. Kats, P. Genevet, N. Yu, Y. Song, J. Kong, and F. Capasso, Broad electrical tuning of graphene-loaded plasmonic antennas, *Nano Lett.* **13**, 1257 (2013).
- [14] M. Z. Alam, S. A. Schulz, J. Upham, I. De Leon, and R. W. Boyd, Large optical nonlinearity of nanoantennas coupled to an epsilon-near-zero material, *Nat. Photonics* **12**, 79 (2018).
- [15] P. C. Wu, R. Sokhyan, G. K. Shirmanesh, W. Cheng, and H. A. Atwater, Near-infrared active metasurface for dynamic polarization conversion, *Adv. Opt. Mater.* **9**, 2100230 (2021).
- [16] J. Sautter, I. Staude, M. Decker, E. Rusak, D. N. Neshev, I. Brener, and Y. S. Kivshar, Active tuning of all-dielectric metasurfaces, *ACS Nano* **9**, 4308 (2015).
- [17] I. Kim, M. A. Ansari, M. Q. Mehmood, W. S. Kim, J. Jang, M. Zubair, Y. K. Kim, and J. Rho, Stimuli-responsive dynamic metaholographic displays with designer liquid crystal modulators, *Adv. Mater.* **32**, 2004664 (2020).
- [18] P. Yu, J. Li, and N. Liu, Electrically tunable optical metasurfaces for dynamic polarization conversion, *Nano Lett.* **21**, 6690 (2021).
- [19] I. Kim, W. S. Kim, K. Kim, M. A. Ansari, M. Q. Mehmood, T. Badloe, Y. Kim, J. Gwak, H. Lee, Y. K. Kim, and J. Rho, Holographic metasurface gas sensors for instantaneous visual alarms, *Sci. Adv.* **7**, eabe9943 (2021).
- [20] M. A. Kats, R. Blanchard, P. Genevet, Z. Yang, M. M. Qazilbash, D. N. Basov, S. Ramanathan, and F. Capasso, Thermal tuning of mid-infrared plasmonic antenna arrays using a phase change material, *Opt. Lett.* **38**, 368 (2013).
- [21] C. Li, X. Hu, W. Gao, Y. Ao, S. Chu, H. Yang, and Q. Gong, Thermo-optical tunable ultracompact chip-integrated 1D photonic topological insulator, *Adv. Opt. Mater.* **6**, 1701071 (2017).
- [22] Z.-Y. Jia, F.-Z. Shu, Y.-J. Gao, F. Cheng, R.-W. Peng, R.-H. Fan, Y. Liu, and M. Wang, Dynamically switching the polarization state of light based on the phase transition of vanadium dioxide, *Phys. Rev. Appl.* **9**, 034009 (2018).
- [23] F. Shu, F. Yu, R. Peng, Y. Zhu, B. Xiong, R. Fan, Z. Wang, Y. Liu, and M. Wang, Dynamic plasmonic color generation based on phase transition of vanadium dioxide, *Adv. Opt. Mater.* **6**, 1700939 (2018).
- [24] Y. Zhang, C. Fowler, J. Liang, B. Azhar, M. Y. Shalaginov, S. Deckoff-Jones, S. An, J. B. Chou, C. M. Roberts, V. Liberman, M. Kang, C. Ríos, K. A. Richardson, C. Rivero-Baleine, T. Gu, H. Zhang, and J. Hu, Electrically reconfigurable non-volatile metasurface using low-loss optical phase-change material, *Nat. Nanotechnol.* **16**, 661 (2021).

- [25] S. Abdollahramezani, O. Hemmatyar, M. Taghinejad, H. Taghinejad, A. Krasnok, A. A. Eftekhar, C. Teichrib, S. Deshmukh, M. A. El-Sayed, E. Pop, M. Wuttig, A. Alù, W. Cai, and A. Adibi, Electrically driven reprogrammable phase-change metasurface reaching 80% efficiency, *Nat. Commun.* **13**, 1696 (2022).
- [26] T. Liu, Z. Han, J. Duan, and S. Xiao, Phase-change metasurfaces for dynamic image display and information encryption, *Phys. Rev. Appl.* **18**, 044078 (2022).
- [27] P. Moitra, Y. Wang, X. Liang, L. Lu, A. Poh, T. W. W. Mass, R. E. Simpson, A. I. Kuznetsov, and R. Paniagua-Dominguez, Programmable wavefront control in the visible spectrum using low-loss chalcogenide phase-change metasurfaces, *Adv. Mater.* **35**, 2205367 (2023).
- [28] S. Chandra, D. Franklin, J. Cozart, A. Safaei, and D. Chanda, Adaptive multispectral infrared camouflage, *ACS Photonics* **5**, 4513 (2018).
- [29] F. Shu, J. Wang, R. Peng, B. Xiong, R. Fan, Y. Gao, Y. Liu, D. Qi, and M. Wang, Electrically driven tunable broadband polarization states via active metasurfaces based on Joule-heat-induced phase transition of vanadium dioxide, *Laser Photonics Rev.* **15**, 2100155 (2021).
- [30] A. Leitis, A. Heßler, S. Wahl, M. Wuttig, T. Taubner, A. Tittl, and H. Altug, All-dielectric programmable Huygens' metasurfaces, *Adv. Funct. Mater.* **30**, 1910259 (2020).
- [31] T. Liu, D. Zhang, W. Liu, T. Yu, F. Wu, S. Xiao, L. Huang, and A. E. Miroshnichenko, Phase-change nonlocal metasurfaces for dynamic wave-front manipulation, *Phys. Rev. Appl.* **21**, 044004 (2024).
- [32] T. Liu, J. Li, and S. Xiao, Single-sized phase-change metasurfaces for dynamic information multiplexing and encryption, *Phys. Rev. Res.* **6**, 023258 (2024).
- [33] F. Ding, S. Zhong, and S. I. Bozhevolnyi, Vanadium dioxide integrated metasurfaces with switchable functionalities at terahertz frequencies, *Adv. Opt. Mater.* **6**, 1701204 (2018).
- [34] W. Chen, R. Chen, Y. Zhou, and Y. Ma, A switchable metasurface between meta-lens and absorber, *IEEE Photonics Technol. Lett.* **31**, 1187 (2019).
- [35] W. Chen, R. Chen, Y. Zhou, R. Chen, and Y. Ma, Spin-dependent switchable metasurfaces using phase change materials, *Opt. Express* **27**, 25678 (2019).
- [36] S. Geiger, J. Michon, S. Liu, J. Qin, J. Ni, J. Hu, T. Gu, and N. Lu, Flexible and stretchable photonics: The next stretch of opportunities, *ACS Photonics* **7**, 2618 (2020).
- [37] S. M. Kamali, A. Arbabi, E. Arbabi, Y. Horie, and A. Faraon, Decoupling optical function and geometrical form using conformal flexible dielectric metasurfaces, *Nat. Commun.* **7**, 11618 (2016).
- [38] M. Zhang, X. Ma, M. Pu, K. Liu, Y. Guo, Y. Huang, X. Xie, X. Li, H. Yu, and X. Luo, Large-area and low-cost nanoslit-based flexible metasurfaces for multispectral electromagnetic wave manipulation, *Adv. Opt. Mater.* **7**, 1900657 (2019).
- [39] J. Cai, C. Zhang, and W. Li, Dual-color flexible metasurfaces with polarization-tunable plasmons in gold nanorod arrays, *Adv. Opt. Mater.* **9**, 2001401 (2020).
- [40] Y. Wang, C. Zhao, J. Wang, X. Luo, L. Xie, S. Zhan, J. Kim, X. Wang, X. Liu, and Y. Ying, Wearable plasmonic metasurface sensor for noninvasive and universal molecular fingerprint detection on biointerfaces, *Sci. Adv.* **7**, eabe4553 (2021).
- [41] J. Wang, B. Xiong, R. Peng, C. Li, B. Hou, C. Chen, Y. Liu, and M. Wang, Flexible phase change materials for electrically tuned active absorbers, *Small* **17**, 2101282 (2021).
- [42] H. Jing, R. Peng, R. M. Ma, J. He, Y. Zhou, Z. Yang, C. Y. Li, Y. Liu, X. Guo, Y. Zhu, D. Wang, J. Su, C. Sun, W. Bao, and M. Wang, Flexible ultrathin single-crystalline perovskite photodetector, *Nano Lett.* **20**, 7144 (2020).
- [43] J. Valentine, J. Li, T. Zentgraf, G. Bartal, and X. Zhang, An optical cloak made of dielectrics, *Nat. Mater.* **8**, 568 (2009).
- [44] X. Liu, J. Wang, L. Tang, L. Xie, and Y. Ying, Flexible plasmonic metasurfaces with user-designed patterns for molecular sensing and cryptography, *Adv. Funct. Mater.* **26**, 5515 (2016).
- [45] H. Hu, X. Guo, D. Hu, Z. Sun, X. Yang, and Q. Dai, Flexible and electrically tunable plasmons in graphene-mica heterostructures, *Adv. Sci.* **5**, 1800175 (2018).
- [46] L. T. Quynh, C.-W. Cheng, C.-T. Huang, S. S. Raja, R. Mishra, M.-J. Yu, Y.-J. Lu, and S. Gwo, Flexible plasmonics using aluminum and copper epitaxial films on mica, *ACS Nano* **16**, 5975 (2022).
- [47] T. Stauber, N. M. R. Peres, and A. K. Geim, Optical conductivity of graphene in the visible region of the spectrum, *Phys. Rev. B* **78**, 085432 (2008).
- [48] K. F. Mak, M. Y. Sfeir, Y. Wu, C. H. Lui, J. A. Misewich, and T. F. Heinz, Measurement of the optical conductivity of graphene, *Phys. Rev. Lett.* **101**, 196405 (2008).
- [49] V. A. Klimov, I. O. Timofeeva, S. D. Khanin, E. B. Shadrin, A. V. Ilinskii, and F. Silva-Andrade, Hysteresis loop construction for the metal-semiconductor phase transition in vanadium dioxide films, *Tech. Phys.* **47**, 1134 (2002).
- [50] X. Xiong, S. Jiang, Y. Hu, R. Peng, and M. Wang, Structured metal film as a perfect absorber, *Adv. Mater.* **25**, 3994 (2013).
- [51] X. Xiong, Z.-H. Xue, C. Meng, S.-C. Jiang, Y.-H. Hu, R.-W. Peng, and M. Wang, Polarization-dependent perfect absorbers/reflectors based on a three-dimensional metamaterial, *Phys. Rev. B* **88**, 115105 (2013).
- [52] R. Honda, M. Ryu, M. Moritake, A. Balčytis, V. Mizeikis, J. Vongsivut, M. J. Tobin, D. Appadoo, J.-L. Li, S. H. Ng, S. Juodkazis, and J. Morikawa, Infrared polariscope imaging of linear polymeric patterns with a focal plane array, *Nanomaterials* **9**, 732 (2019).
- [53] R. A. Hummel, Image enhancement by histogram transformation, *Comput. Graphics Image Process.* **6**, 184 (1977).